Published by IOP Publishing for Sissa Medialab

Received: *May 15, 2026*
Revised: *August 21, 2026*
Accepted: *October 23, 2026*
Published: *November 6, 2026*

Liquid argon purification and purity monitoring: apparatus and first results

W.-Z. Wei,[a,*] **I.W. Jaidee,**[a,1] **S. Dockal,**[a,2] **V. Tsvetkova,**[a] **G. Bui,**[a] **T. Chen Lin,**[a] **L. Epstein,**[a] **A. Faubus,**[a] **N.M.T. Hambraeus,**[a] **S.B. Lyon,**[a] **D. Lopez,**[a] **N. McGee,**[a] **P.J. Migden,**[a] **C. Nicollin,**[a] **M. Unnithan,**[a] **J. Asaadi**[b] **and J.B.R. Battat**[a]

[a] *Department of Physics and Astronomy, Wellesley College, 106 Central St., Wellesley, MA 02481, U.S.A.*
[b] *Department of Physics, University of Texas at Arlington, 502 Yates St., Arlington, TX 76019, U.S.A.*

E-mail: ww102@wellesley.edu

Abstract: We report results from a 13-liter purified liquid argon test stand at Wellesley College in Massachusetts, U.S.A.. The system includes a single-pass liquid-phase purification column that can achieve sub-part-per-billion impurity levels. The liquid argon purity is measured with a double-gridded purity monitor to assess the electron lifetime. Measurements demonstrate an O_2-equivalent impurity concentration of 0.21 ± 0.05 ppb (stable over a 20-hour duration), corresponding to an electron lifetime of 1.6 ms at a drift field of 500 V/cm. This test stand supports ongoing detector R&D on charge and light readout for liquid argon time projection chambers, such as Q-Pix and other cold electronics systems.

Keywords: Cryogenic detectors; Neutrino detectors

ArXiv ePrint: 2604.21307

[*] Corresponding author.
[1] Current address: Department of Physics, Harvard University, Cambridge, MA 02138, U.S.A.
[2] Current address: Department of Physics, Syracuse University, Syracuse, NY 13244, U.S.A.

© 2026 The Author(s). Published by IOP Publishing Ltd on behalf of Sissa Medialab. Original content from this work may be used under the terms of the Creative Commons Attribution 4.0 licence. Any further distribution of this work must maintain attribution to the author(s) and the title of the work, journal citation and DOI.

https://doi.org/10.1088/1748-0221/21/11/P11007

Contents

1 Introduction **1**

2 System overview **2**
- 2.1 The single-pass liquid-phase purifier 2
- 2.2 The cryostat and purity monitor 6
- 2.3 Slow control and data acquisition system 7

3 Experimental procedures **8**
- 3.1 Purifier regeneration 8
- 3.2 LAr filling 9

4 System performance **10**
- 4.1 Waveform acquisition and modeling 10
- 4.2 Measured drift time, electron lifetime and impurity concentration 11

5 Discussion and conclusion **14**

2026 JINST 21 P11007

1 Introduction

Liquid argon time projection chambers (LArTPCs) have become a prominent technology for neutrino and rare-event physics due to their excellent spatial resolution, calorimetric capabilities, and scalability [1–3]. They are used in several current and future large-scale experiments, including dark matter searches such as DarkSide-20k [4], as well as neutrino experiments such as ICARUS [5], MicroBooNE [6], SBND (Short-Baseline Near Detector) [7], and the Deep Underground Neutrino Experiment (DUNE) [8].

In a LArTPC, charged particles traversing liquid argon (LAr) produce ionization electrons and scintillation light. Under an applied electric field, the ionization electrons drift toward a readout plane, where their 2D arrival positions combined with the differences in arrival times provide a full 3D reconstruction of the ionization distribution within the LArTPC. When the absolute drift time is known from the prompt scintillation light, the absolute position of the interaction vertex along the drift direction can also be measured, allowing full-volume fiducialization. In addition to imaging the event topology, the collected ionization charge provides a measurement of the energy deposited by the particle along its path. After correcting for effects such as electron attenuation and recombination, the charge per unit length can be converted to deposited energy, enabling calorimetric energy reconstruction and particle identification.

The successful operation of LArTPCs critically depends on maintaining ultra-high purity of the LAr to prevent degradation of scintillation and ionization yields [9]. Nitrogen and oxygen quench argon excimer states and thereby reduce the scintillation light yield [10, 11], while oxygen and water absorb vacuum ultraviolet (VUV) photons [11, 12]. In addition, drifting electrons may attach to electronegative impurities (primarily H_2O and O_2), attenuating the ionization signal [13]. The electron

lifetime is commonly used as a performance benchmark. At a typical drift field of 500 V/cm,[1] the electron drift velocity in LAr is 1.6 mm/µs [14]. For large-scale detectors with drift distances of several meters, this corresponds to electron transit times of many milliseconds. Achieving adequate electron drift lifetimes requires impurity concentrations below a part-per-billion (ppb), which is several orders of magnitude lower than commercially available in ultra-high-purity (UHP) LAr. Consequently, ensuring and continuously monitoring argon purity remains a central priority in LArTPC operation.

Several LAr purification and purity monitoring systems have been built, including the Liquid Argon Purity Demonstrator (LAPD) [15] and Luke (also known as the Materials Test Stand (MTS)) [16] at Fermilab, ARGONTUBE [17, 18] at the University of Bern, and more recent large-scale R&D prototypes such as CAPTAIN [19] at Los Alamos and protoDUNE-SP [20] at CERN. These facilities generally employ continuous LAr recirculation through dedicated filters to remove impurities, which allows efficient purification of large volumes, along with purity monitors to track the electron lifetime. In the most widely used purity monitor design, developed by the ICARUS collaboration [21], ultraviolet (UV) light liberates electrons from a photocathode via the photoelectric effect. A uniform electric field drives the resulting electrons toward an anode, and the electron lifetime is determined from the attenuation of the electron signal. The design and operation of the UV-based purity monitor (UV-PrM) is described in detail in ref. [22]. In this work, we report on the design, construction, operation and performance of a LAr test stand at Wellesley College that uses a single-pass purifier to remove the electronegative contaminants O_2 and H_2O, and a UV-PrM to measure and monitor the LAr purity. This test stand supports ongoing detector R&D for novel LArTPC charge and light readout technologies such as Q-Pix [23, 24].

This paper is organized as follows. Section 2 details the design of the purifier and UV-PrM. Section 3 discusses our experimental procedures. Section 4 describes the data acquisition system and presents our experimental results. Finally, section 5 summarizes the results, lessons learned, and future plans.

2 System overview

Figure 1 shows the piping and instrumentation diagram (P&ID) and photograph of the system, which consists of a single-pass purifier, a cryostat housing a UV-PrM along with associated hardware and a vacuum pumping station. A slow-control and data acquisition system allows for remote monitoring of the apparatus.

LAr purification occurs in the liquid phase during the filling of the cryostat. LAr flows from a dewar of commercially available ultra high purity liquid argon (typically with oxygen and water contamination levels of 0.1 and 1 ppm, respectively) through the purifier, and into the cryostat that houses the UV-PrM. Each sub-system is described in more detail below.

2.1 The single-pass liquid-phase purifier

The single-pass liquid-phase purifier consists of two filters in series, as shown in figure 2. The first filter contains 0.3 kg of 4 Å molecular sieve (MS) in a 8.25 inch-long 4.5″ ConFlat (CF) nipple. The MS is primarily responsible for removing water, but it can also remove small amounts of nitrogen and residual oxygen. The second filter consists of 1.7 kg of activated copper (AC)

[1] A drift field of 500 V/cm is commonly chosen in LArTPCs to balance scintillation and ionization signal yields.

2026 JINST 21 P11007

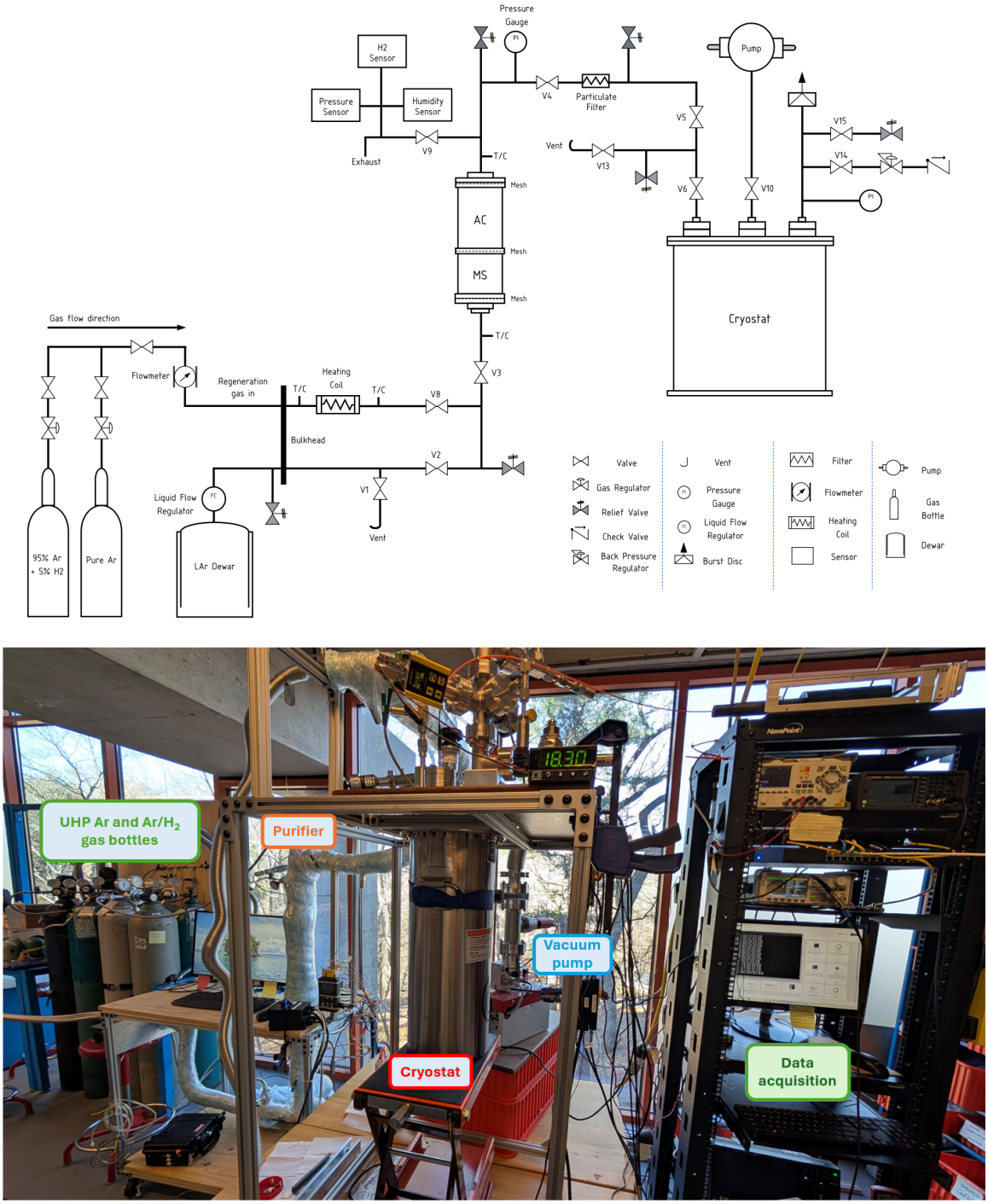


Figure 1. *Top:* P&ID diagram of the system. *Bottom:* photograph of the experimental setup, showing the gas bottles used for purifier regeneration, the purification column, the vacuum pump station, the cryostat housing the purity monitor, and the data acquisition system. The xenon flash lamp and control electronics are located at the top of the electronics rack. LAr flows upward through the purifier column before entering the cryostat.

2026 JINST 21 P11007

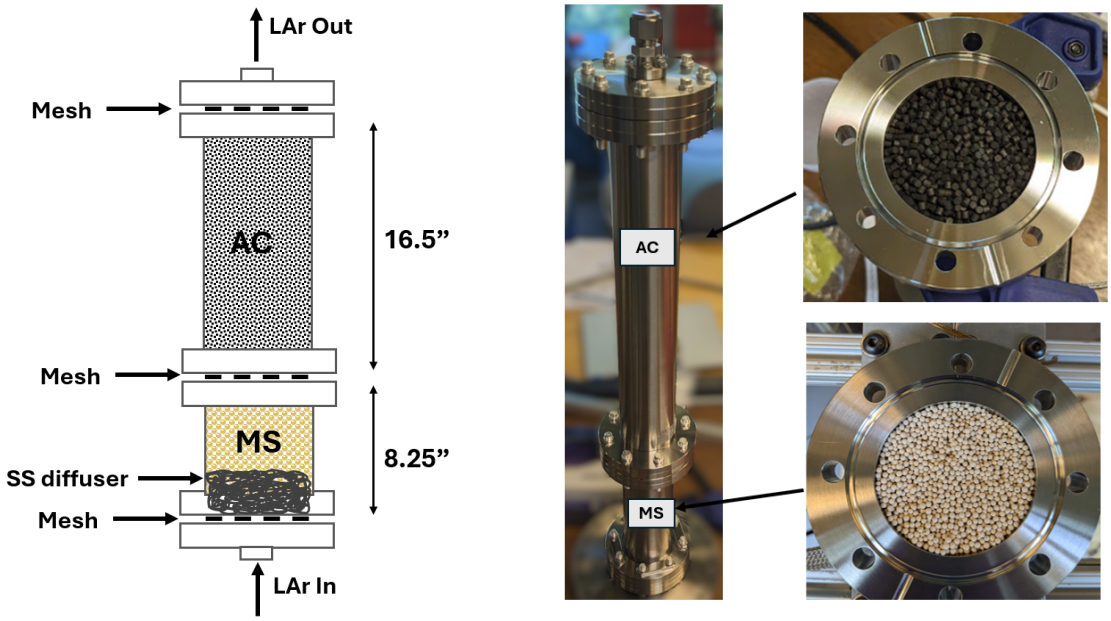


Figure 2. *Left:* schematic diagram of the purification column. *Right:* photograph of the purifier with the interior view of the AC catalyst pellets, which appear black due to oxidation (copper-colored after regeneration), and the MS beads.

catalyst in a 16.5 inch-long 4.5″ CF nipple and is used primarily for oxygen removal and, to a lesser extent, for water removal. A stainless steel (SS) mesh between the two nipples prevents filter media mixing. Throughout this paper we refer to the two filter media as the MS column and the AC column.

The purifier performance depends on several factors, including liquid-filter contact, flow rate, purifier material capacity and regeneration, as well as system cleanliness, outgassing, and thermal stability. To maximize contact between the liquid and the filter media and to prevent channeling, a SS diffuser was installed at the purifier inlet (see figure 3, left). The diffuser, together with a controlled flow rate, helps distribute the LAr more evenly throughout the filter media, improving contact with the purifier materials. To mechanically secure the diffuser and prevent the MS beads from escaping the column, a SS mesh was placed above the diffuser (figure 3, right).

Temperature monitoring and control are critical during both regeneration and LAr purification. The purifier is instrumented with eight K-type thermocouples (see figure 4(a)) to monitor the temperature at various locations during both regeneration and LAr flow: four are embedded within the column volume, and four are attached to the exterior surfaces of the two CF nipples. Also shown in panel (a) of figure 4 are two heater tapes wrapped around the columns, each controlled by a “bang-bang” (on-off) heater controller, which heats the column during filter regeneration (section 3.1). Figure 4 also shows the two layers of insulation used to reduce heat exchange with the environment and improve thermal stability: aluminum foil (b) and Cryo-Lite fiberglass (c). The insulation serves dual purposes: during LAr purification, it minimizes heat transfer to limit boil-off and maintain uniform flow; during purifier regeneration, it allows the column to reach and sustain target temperatures efficiently, enhancing the effectiveness of the regeneration. Panel (d) of figure 4 shows plastic wrap applied outside the Cryo-Lite fiberglass, which serves as a moisture barrier to prevent condensation on the fiberglass insulation.

2026 JINST 21 P11007



Figure 3. Stainless steel diffuser (left) and mesh (right) were installed at the purifier entrance, where LAr flows into the MS column.



Figure 4. Purification column exterior with (a) heater tapes and thermocouples covered with (b) aluminum foil, (c) Cryo-Lite fiberglass insulation, and (d) plastic wrap as a vapor barrier.

In addition to the thermocouples, heater tapes, and insulation layers, the purifier is instrumented with a pressure sensor, a humidity sensor, and a hydrogen concentration monitor (Nova Analytical Systems Model 5000-335-JK) to track the status of the regeneration process. These sensors provide information on the pressure, water content, and hydrogen content of the gas flowing through the filter media. Further details are provided in section 3.1.

2026 JINST 21 P11007

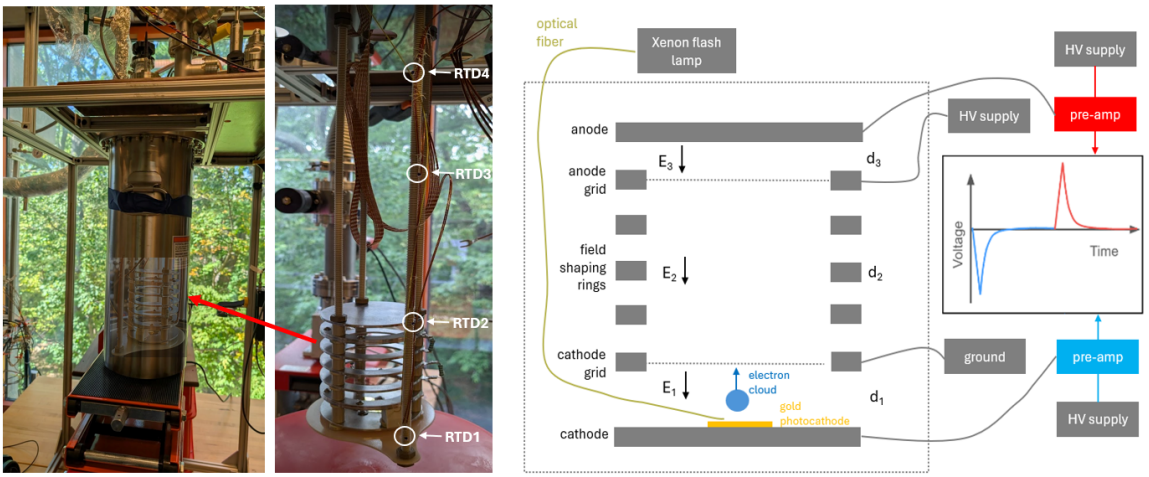


Figure 5. *Left:* cryostat with overlay showing the location of the UV-PrM. *Middle:* UV-PrM and locations of the RTDs. *Right:* schematic diagram of the UV-PrM showing the optical and electrical connections.

2.2 The cryostat and purity monitor

The cryostat is a 13-liter cylindrical vacuum jacketed dewar (Cryofab CF7518) with an internal depth of 18 in, an inner diameter of 7.45 in, and a 10-inch CF flange. The cryostat is sealed with a six-port, 10-inch CF top plate (Kurt J. Lesker CF1000S6). The six ports on the top plate accommodate LAr and gas inlets, the vacuum pump, optical fiber for UV light injection, high-voltage and signal lines, resistive temperature detectors (RTD) to monitor the LAr level, and multiple pressure gauges and pressure management devices including a back-pressure regulator with a check valve, a pressure relief valve, a burst disk, and several pressure sensors: an ion gauge, a convectron gauge, a dial gauge, and an absolute pressure transducer used to monitor the internal cryostat pressure.

As shown in figure 5, the UV-PrM is suspended from the top plate of the cryostat and fully immersed in LAr during operation. Four RTD sensors positioned at different heights in the chamber provide temperature and liquid level monitoring during operation. A baffle between the field cage and the top plate reduces thermal loading.

The UV-PrM includes three regions of uniform electric field: between the cathode and cathode grid (cathode region), the cathode grid and anode grid (drift region), and the anode grid and anode (anode region), with respective lengths of 1.9 cm, 5.8 cm, and 1.2 cm. Both grids are electroformed copper meshes (MC7 25LPI copper mesh by Precision Eforming) held in tension between two SS rings. Electric field uniformity in the drift region is maintained by three field-shaping rings connected by 50 MΩ resistors. The electrode geometry was simulated using the *FreeFEM* finite element analysis software to verify the uniformity of the drift field within the active volume (see figure 6). In the central region of the PrM, where the signal electrons are generated and drift, the field uniformity is better than 2% ($\Delta E/E < 0.02$).

Electrons are produced at a photocathode via the photoelectric effect: ultraviolet light from a pulsed 60 W xenon flash lamp (Hamamatsu L7685) is transmitted via optical fiber to a piece of gold-coated silicon attached (mechanically and electrically) to the cathode (see figure 5). The liberated electrons drift upward through the cathode grid toward the anode. The drifting electrons in the cathode

2026 JINST 21 P11007

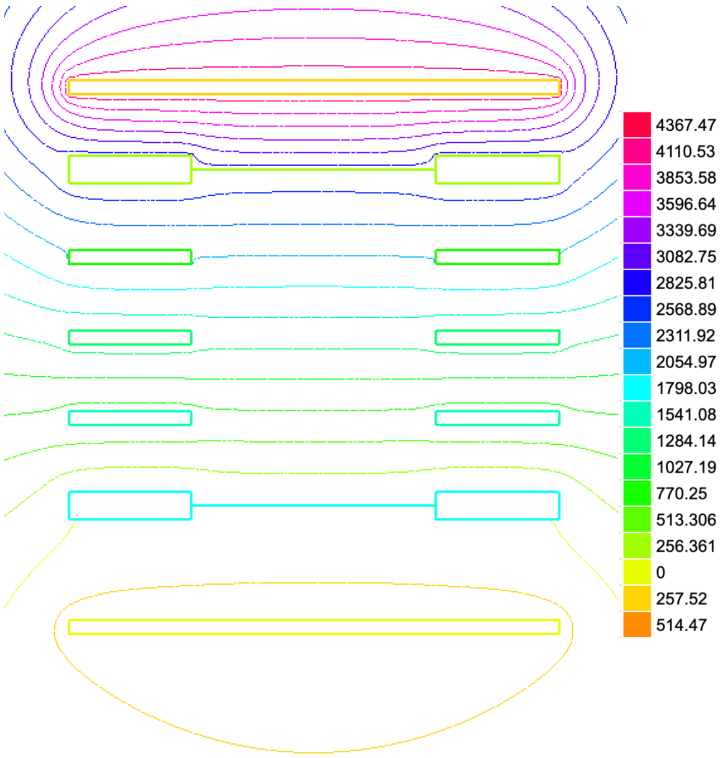


Figure 6. A 2D cross-section equipotential field map of the purity monitor made using the FreeFEM finite element software. The lines are color-coded based on the electric potential in volts.

region induce a current on the cathode. Likewise they induce a current on the anode electrode when drifting in the anode region. The grids electrically isolate the cathode and anode from induced signals when the electrons traverse the drift region. Appropriately large field ratios E_3/E_2 and E_2/E_1 are chosen to ensure that the grids are transparent to the drifting electrons [22].

The induced charge at the anode (Q_A) and cathode (Q_C) are measured using charge-sensitive preamplifiers (Cremat CR-110-R2). Any deficit in Q_A relative to Q_C is attributed to electron capture by impurities in the LAr, and the ratio Q_A/Q_C provides a direct measure of the electron lifetime and impurity concentration in the LAr.

2.3 Slow control and data acquisition system

A slow control system monitors and records environmental and system operating parameters. The sensors include a drum scale to monitor the weight of LAr inside the supply dewar, a humidity sensor, pressure sensor, hydrogen concentration sensor, and thermocouples for the purifier, and pressure sensors and four RTDs for the cryostat. The sensors are connected to serial-to-ethernet adapters (Waveshare RS232/485 to ethernet) providing TCP/IP accessibility via static IP addresses. The Detector OBservation and Error Reporting Multiadaptive ApplicatioN (Doberman) software [25] handles the sensor communication and data logging to an Influx database. Data are viewable via the web using Doberview [26] (see figure 7). For the LAr measurements reported in this paper some sensors (purifier thermocouples and the H_2 monitor) were logged independently of Doberman.

2026 JINST 21 P11007

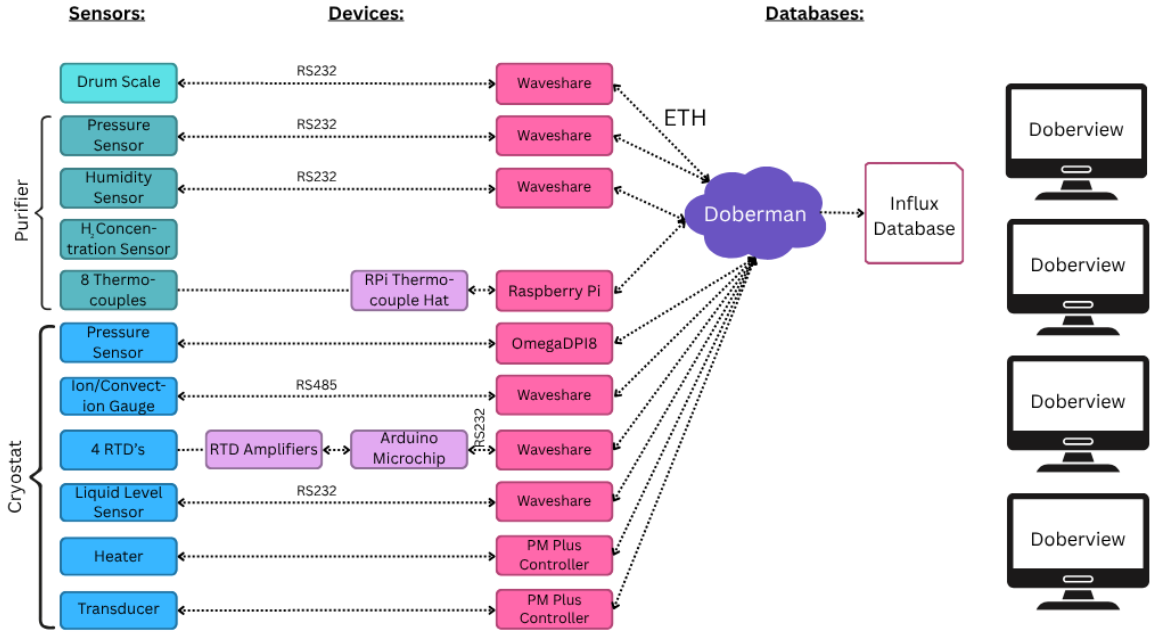


Figure 7. Diagram of slow control connectivity showing the interface devices between sensors and Doberman. Doberview, running on remote machines, is used to display slow control data.

3 Experimental procedures

3.1 Purifier regeneration

The MS and AC filter media initially have significant adsorbed water and oxygen and therefore require initial regeneration prior to first use. The regeneration procedure (i) desorbs water from the MS and (ii) chemically reduces oxidized copper (CuO) to metallic copper (Cu) in the catalyst via the reaction:

$$\mathrm{CuO} + \mathrm{H_2} \rightarrow \mathrm{Cu} + \mathrm{H_2O}. \tag{3.1}$$

The purifier was designed to filter 1000 L of LAr before needing to be regenerated, though we typically perform regeneration one day prior to each LAr run to ensure optimal purifier performance.

The purifier is regenerated through a three-stage procedure: preheating, hydrogen-assisted regeneration, and finally, cooldown and sealing. Figure 8 shows sensor data from a filter regeneration during all three stages of the process.

1. **Preheating.** Ultra-high-purity (UHP) gas Ar is flowed through the purifier as the purifier is heated until the exhaust temperature reaches 180 °C. During this stage water desorbs from the MS and is flushed out by the Ar flow.

2. **Hydrogen-assisted regeneration.** Once the target temperature is reached, the inlet gas is switched from UHP Ar to a Ar/H_2 mixture (95%/5%). The onset of hydrogen flow further increases the exhaust temperature due to the exothermic reduction of CuO. Likewise the exhaust gas humidity rises sharply since water is a byproduct of the reduction reaction. The Ar/H_2 flow rate is then reduced to ensure that the temperature of the filter media remains below 220 °C

2026 JINST 21 P11007

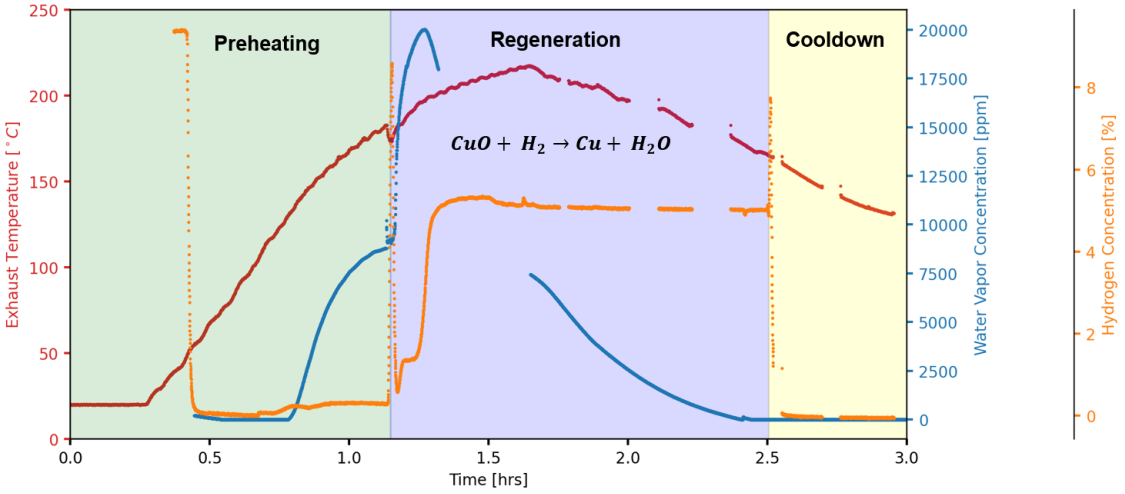


Figure 8. Temperature at the purifier outlet, along with water vapor and hydrogen concentration in the exhaust gas during filter regeneration. The cooldown stage continued for two hours beyond what is shown here. The gap in the water vapor data was caused by unexpected downtime of the Doberman slow-control system (at the time of this run, the temperature and water vapor data were logged separately from Doberman).

to avoid damaging the AC. The MS and AC regeneration is considered complete once (i) the H_2 concentration in the exhaust gas returns to the input level (5%), indicating that hydrogen is no longer being consumed in the reduction reaction and (ii) the water vapor concentration at the outlet decreases to zero indicating that the water has been desorbed from the MS. In our system, fully saturated filter media (as received from the vendor) requires about 12 hours for regeneration, while a substantially shorter cycle (15–30 min) can "top up" recently recharged filter media.

3. **Cooldown and sealing.** Once the regeneration stage is complete, the inlet gas is switched back to UHP Ar and the heaters are turned off. UHP Ar is flowed at a high rate to cool the column, at which point the system is overpressurized by about 5 psig with UHP Ar and sealed in preparation for future LAr purification.

3.2 LAr filling

Before each LAr run, we do several pump-and-purge cycles to reduce residual impurities in the cryostat and liquid transfer lines. The system is first evacuated below 10^{-4} torr and then backfilled with UHP Ar to 5–7 psig at room temperature. This sequence is repeated three to four times to dilute and remove contaminants released from internal surfaces. After the final purge, the chamber is pumped down once more and held under vacuum in preparation for the LAr fill.

Because the section of the liquid transfer line between the LAr storage dewar and purification column cannot be evacuated during the pump-and-purge cycles, it may contain residual contaminants. To minimize the transport of these contaminants into the chamber, the transfer line is purged through vents (near valves V1 and V13 in figure 1). Once a steady liquid stream is observed at V13, the flow is redirected into the chamber.

2026 JINST 21 P11007

During filling, the internal pressure of the cryostat is regulated by the pressure relief valve on the top plate. The liquid level inside the cryostat is monitored using the RTDs. Filling is stopped once all four RTDs show stable LAr temperatures, after which the pressure relief valve is sealed to prevent potential backflow contamination. The back-pressure regulator (with check valve) maintains a stable head pressure in the cryostat as the LAr slowly evaporates.

4 System performance

The LAr purity is measured with a UV-PrM. A digital oscilloscope controlled by a custom Python script records waveforms from the cathode and anode charge-sensitive preamplifiers (CSP); the electron lifetime and LAr purity are determined as described below.

4.1 Waveform acquisition and modeling

During PrM operation, the xenon flash lamp repetition rate is typically 10 Hz. To reduce noise in the CSP waveforms, we average hundreds of individual triggers on the oscilloscope and then record the averaged waveforms for offline analysis. A typical pair of averaged cathode and anode waveforms is shown in figure 9. The start of the rising edge of each pulse corresponds to the moment when the electrons enter the respective cathode or anode region (labeled "1" for the cathode waveform and "5" for the anode). The integral of the waveform is proportional to the total charge collected:

$$Q_C \propto \int V_C(t)\,dt, \qquad Q_A \propto \int V_A(t)\,dt. \tag{4.1}$$

We observe an unexpected feature (a "bump") in the anode waveform prior to the main anode peak. This feature is consistently present and has the characteristic CSP decay timescale, but it occurs too early to be generated by electrons in the anode region. We attribute it to parasitic capacitive coupling in the PrM. Our analysis accounts for the impact of this signal on the measurement of Q_A.

We define three time intervals (indicated visually in figure 9):

- $T_1 = t_{\mathrm{c,peak}} - t_{\mathrm{c,start}}$: electron drift time from the cathode to the cathode grid;
- $T_2 = t_{\mathrm{a,start}} - t_{\mathrm{c,peak}}$: electron drift time from the cathode grid to the anode grid;
- $T_3 = t_{\mathrm{a,peak}} - t_{\mathrm{a,start}}$: electron drift time from the anode grid to the anode.

The total electron drift time is then [27]:

$$t_{\mathrm{drift}} = T_2 + \frac{T_1 + T_3}{2}, \tag{4.2}$$

which accounts for the average time electrons spend in the cathode (T_1) and anode (T_3) regions and the full drift time, T_2, in the drift region between the grids.

We model the cathode and anode waveforms as the convolution of the CSP impulse response function (an exponential decay with time constant τ_f) with a constant current of duration T [27]:

$$V_{\mathrm{out}}(t) = \begin{cases} h_0\, Q\, \dfrac{\tau_f}{T}\left(1 - e^{-t/\tau_f}\right), & t < T, \\ h_0\, Q\, \dfrac{\tau_f}{T}\left(e^{T/\tau_f} - 1\right) e^{-t/\tau_f}, & t \geq T. \end{cases} \tag{4.3}$$

2026 JINST 21 P11007

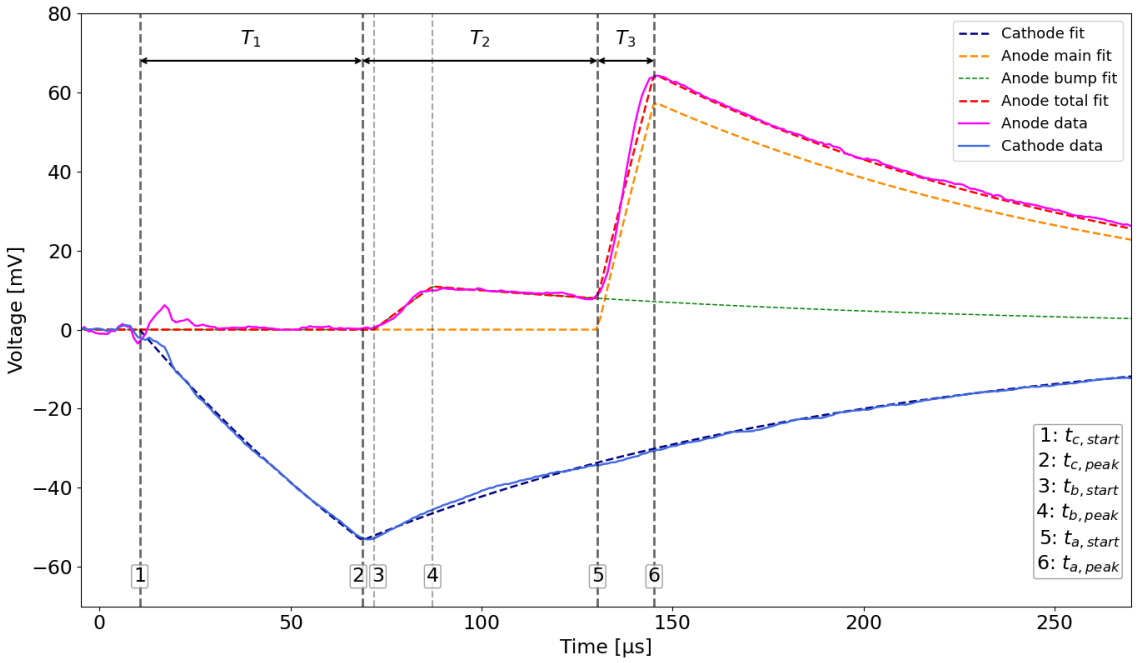


Figure 9. Example cathode and anode waveforms along with fitted model components. The drift times T_1, T_2, and T_3 are indicated on the plot. The relevant times for the two-component model used for the anode signal, as well as the times for the cathode signal are also indicated.

The decay time constant is the product of the resistance and capacitance in the feedback loop of the CSP: $\tau_f = R_f C_f$. Independent measurements of τ_f for the two CSPs provide *a priori* constraints on those parameters (133 μs and 135 μs for anode and cathode, respectively). Our Cremat CR-110 CSPs include a secondary voltage amplification stage with a gain of two, so $h_0 = \pm 2/C_f$ (with the minus sign for the cathode signal). We use a non-linear least-squares minimization to fit Eq. 4.3 to our data, with free parameters Q (the total charge collected: Q_C for cathode and Q_A for anode), the "turn-on time" t_{start} ($t_{\text{c,start}}$ for the cathode and $t_{\text{a,start}}$ for the anode), and the duration of the current pulse T (T_1 for the cathode and T_3 for the anode). Our model of the anode data includes two components: one for the bump, and the second for the anode signal of interest:

$$V_A(t) = V_A^{\text{anode}}(t - t_{\text{a,start}}) + V_A^{\text{bump}}(t - t_{\text{b,start}}). \tag{4.4}$$

In sum, our models for the cathode and anode waveforms are:

$$V_C(t) = V_C\big(t, [\, t_{\text{c,start}},\, t_{\text{c,peak}},\, Q_{\text{C}}]\big)\,, \tag{4.5}$$

$$V_A(t) = V_A\big(t, [\, t_{\text{a,start}},\, t_{\text{a,peak}},\, Q_{\text{A,anode}},\, t_{\text{b,start}},\, t_{\text{b,peak}},\, Q_{\text{A,bump}}]\big)\,, \tag{4.6}$$

where the terms in the square brackets are the fit parameters.

4.2 Measured drift time, electron lifetime and impurity concentration

We present three analyses using data from our PrM. The first is a consistency check comparing the measured and predicted electron drift times in the PrM. The second is a quantitative measurement of the LAr purity level over a 20-hour period of time. The third is, to our knowledge, a novel way

2026 JINST 21 P11007

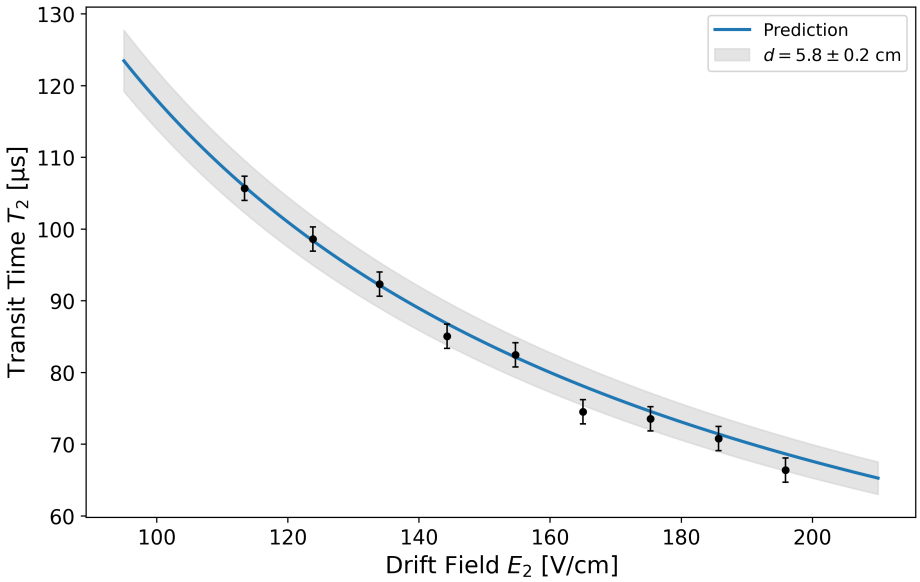


Figure 10. Measured and predicted drift region transit times T_2 as a function of the drift field E_2. The shaded band accounts for the systematic error due to a 2 mm uncertainty in the drift distance.

to estimate the LAr purity by scanning the electric field strengths in the PrM. The main result is that with our single-pass purifier, we achieve sub-ppb oxygen-equivalent impurity concentration in the LAr, stable over the course of at least a day.

First we compare the measured and predicted transit times T_2 of the electrons in the drift region as a function of the drift electric field E_2. The predicted transit time is given by the ratio of the drift distance d_2 and the drift speed $v_{\text{drift}} = \mu E_2$, where the mobility μ of electrons in LAr is itself dependent on both E_2 and the LAr temperature T_{LAr} [14]:

$$T_2 = \frac{d_2}{v_{\text{drift}}} = \frac{d_2}{\mu(E_2, T_{LAr})E_2}. \tag{4.7}$$

As seen in figure 10 we find good agreement between measured and predicted electron transit times. This reinforces the interpretation that the cathode and anode signals $V_{\text{C}}(t)$ and $V_{\text{A}}^{\text{anode}}(t)$ are generated by electrons from the photocathode drifting through the cathode and anode regions, respectively. It also supports our claim that $V_{\text{A}}^{\text{bump}}(t)$ is not generated by electrons in the anode region.

Next, we measure the electron lifetime τ directly from the measured charge survival fraction $Q_{\text{A,anode}}/Q_C$ and electron drift time using [27]:

$$\frac{Q_{\text{A,anode}}}{Q_C} = e^{-t_{\text{drift}}/\tau}. \tag{4.8}$$

Notice that the numerator of the charge survival fraction does not include any contribution from the bump. We repeated this measurement over the course of one day (see figure 11), finding that the lifetime remained stable. The weighted average lifetime of these measurements is

$$\tau = (1.24 \pm 0.02)\ \text{ms}, \tag{4.9}$$

where the reported uncertainty is the standard error on the mean.

2026 JINST 21 P11007

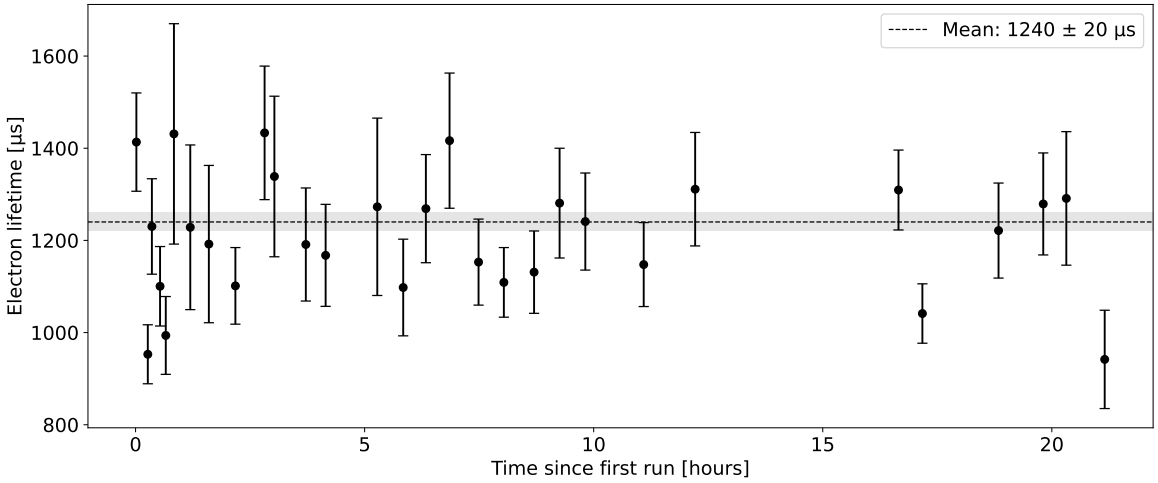


Figure 11. Electron lifetime over a 21-hour period with drift field $E_2 = 160\,\mathrm{V/cm}$. The horizontal dashed line gives the weighted average lifetime over the full time span. The gray band indicates the standard error on the mean.

We then compute the LAr impurity concentration from the measured lifetime. From our measurements of Q_A and Q_C alone, we cannot disentangle the contributions of underlying impurity species (e.g. oxygen vs. water vs. nitrogen), so we follow standard practice and report the oxygen-equivalent impurity concentration n_{O_2} using the approach of ref. [28]:

$$n_{O_2} = \frac{1}{k_{O_2}\,\tau}, \tag{4.10}$$

where k_{O_2} is the impurity attachment coefficient of oxygen. The attachment coefficient depends on electric field. At our operating field of 160 V/cm, we use $k_{O_2} = (3.84 \pm 0.86) \times 10^{12}\,\mathrm{s}^{-1}$, which comes from the rational polynomial parameterization (for impurity species A) from ref. [28]:

$$k_A = 10^p \cdot \frac{\frac{a_1}{b_1} + a_1 E + a_2 E^2 + a_3 E^3 + a_4 E^4}{1 + b_1 E + b_2 E^2 + b_3 E^3 + b_4 E^4}, \tag{4.11}$$

with E the electric field in units of kV/cm (and k_A in units of s^{-1}). The coefficients p, a_i and b_i for oxygen are also provided in ref. [28]. The associated uncertainty on k_{O_2} is obtained from figure 1 of the same reference. The resulting oxygen-equivalent impurity concentration is

$$n_{O_2} = (0.21 \pm 0.05)\,\mathrm{ppb}, \tag{4.12}$$

where the error is predominantly due to the uncertainty in k_{O_2}.

Finally, we measure the charge survival fraction as a function of drift field E_2, which provides a semi-quantitative estimate of the electronegative impurity concentration in the LAr. As we varied the drift field E_2 in this study, we also adjusted the cathode and anode electric fields E_1 and E_3 to maintain field ratios E_3/E_2 and E_2/E_1 above 2 for stable mesh transparency [27]. Figure 12 shows the result along with the predicted Q_A/Q_C for a range of oxygen-equivalent impurity levels. The comparison suggests an oxygen-equivalent impurity level of 0.2 to 0.3 ppb, consistent with the impurity concentration measurement at $E_2 = 160\,\mathrm{V/cm}$ presented earlier.

2026 JINST 21 P11007

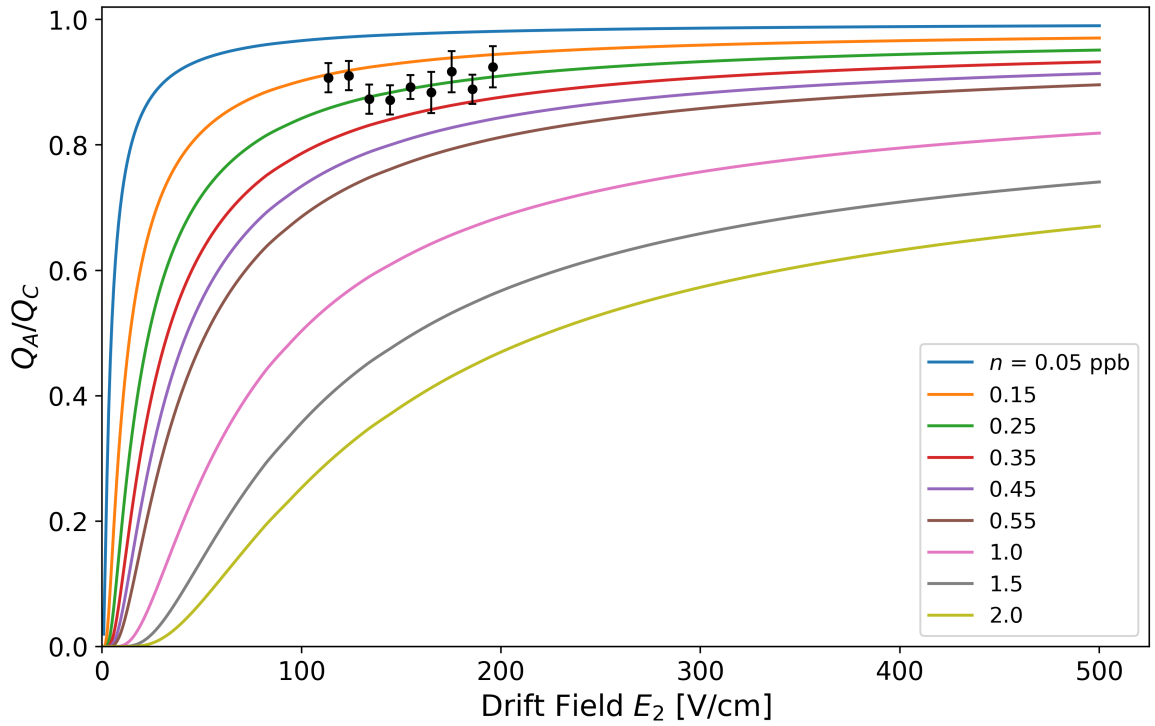


Figure 12. Charge ratio Q_A/Q_C and theoretical predictions for O_2 concentrations as a function of the drift field E_2.

5 Discussion and conclusion

In summary, a compact 13-liter LAr test stand featuring a single-pass liquid-phase purifier and a UV-PrM has been successfully constructed and operated at Wellesley College. System performance was evaluated through drift-field scans and long-term purity measurements. The measured electron drift speeds are consistent with theoretical predictions, validating the UV-PrM configuration and timing analysis. The electron lifetime remained stable at 1.2 ms (E_2 = 160 V/cm) for more than 20 hours of continuous operation, demonstrating both the effectiveness of the purifier and the stable operation of the UV-PrM and cryogenic system. Data taking ultimately ended due to LAr boiloff, not degradation in purity. The measured electron lifetime corresponds to an O_2-equivalent impurity concentration of 0.2 ppb, which yields an electron lifetime of 1.6 ms at a drift field of 500 V/cm. These results demonstrate that the system can produce stable sub-ppb impurity levels and millisecond-scale electron lifetimes.

Based on the experience gained with this 13-liter cryostat, we have built a larger version (250-liter), which employs the same UV-PrM design alongside a LArTPC to serve as platform for R&D on Q-Pix and other LArTPC readout technologies. We have begun using the larger cryostat, fed by the same purification column used in this paper. Our first run achieved n_{O_2} = 0.4 ppb. While we certainly expect improvements as we identify and eliminate impurity sources, this level of purity already exceeds our specification for the planned detector R&D work as it corresponds to an electron drift distance of more than one meter at 500 V/cm. At this time we do not have a need for LAr recirculation system, though the apparatus could be upgraded to include one should the need arise.

2026 JINST 21 P11007

Acknowledgments

We thank Yichen Li (Brookhaven National Lab) and Yun-Tse Tsai (SLAC), as well as Michael Mooney and Sam Fogarty (Colorado State University) for their valuable support and discussions about purifier and purity monitor design and operation. We also thank Lindsay Donovan (Wellesley College) for her contribution to the measurements of the field cage. We acknowledge significant contributions by Larry Knowles (Wellesley College, deceased) to the mechanical design, machining and system assembly. This work was supported by the Gordon and Betty Moore Foundation (Grant No. GBMF11565 with DOI https://doi.org/10.37807/GBMF11565) and by the U.S. Department of Energy through the FAIR award DE-SC0024323. The publication fees for this article were supported by the Wellesley College Library and Technology Services Open Access Fund.

References

[1] C. Rubbia, *The Liquid Argon Time Projection Chamber: A New Concept for Neutrino Detectors*, CERN-EP-INT-77-08 (1977).

[2] K. Majumdar and K. Mavrokoridis, *Review of Liquid Argon Detector Technologies in the Neutrino Sector*, *Appl. Sciences* **11** (2021) 2455 [arXiv:2103.06395].

[3] A.B. McDonald, *Dark matter detection with liquid argon*, *Nucl. Phys. B* **1003** (2024) 116436.

[4] DarkSide-20k collaboration, *DarkSide-20k: A 20 tonne two-phase LAr TPC for direct dark matter detection at LNGS*, *Eur. Phys. J. Plus* **133** (2018) 131 [arXiv:1707.08145].

[5] V. Pia, *Status and Perspective of ICARUS at the Fermilab Short-Baseline Neutrino Program*, *Springer Proc. Phys.* **425** (2025) 117.

[6] MicroBooNE collaboration, *Design and Construction of the MicroBooNE Detector*, 2017 *JINST* **12** P02017 [arXiv:1612.05824].

[7] SBND collaboration, *The Short-Baseline Near Detector at Fermilab: Input to the European Strategy for Particle Physics 2026 Update*, arXiv:2504.00245.

[8] DUNE collaboration, *Deep Underground Neutrino Experiment (DUNE), Far Detector Technical Design Report, Volume I Introduction to DUNE*, 2020 *JINST* **15** T08008 [arXiv:2002.02967].

[9] C. Vogl et al., *A liquid-phase loop-mode argon purification system*, 2024 *JINST* **19** C03030 [arXiv:2311.18697].

[10] WArP collaboration, *Effects of Nitrogen contamination in liquid Argon*, 2010 *JINST* **5** P06003 [arXiv:0804.1217].

[11] WArP collaboration, *Oxygen contamination in liquid Argon: Combined effects on ionization electron charge and scintillation light*, 2010 *JINST* **5** P05003 [arXiv:0804.1222].

[12] R. Onaka and T. Takahashi, *Vacuum UV Absorption Spectra of Liquid Water and Ice*, *J. Phys. Soc. Jap.* **24** (1968) 548.

[13] G. Bakale, U. Sowada and W.F. Schmidt, *Effect of an electric field on electron attachment to sulfur hexafluoride, nitrous oxide, and molecular oxygen in liquid argon and xenon*, *J. Phys. Chem.* **80** (1976) 2556.

[14] BNL, *Liquid Argon Properties*, https://lar.bnl.gov/properties/.

[15] M. Adamowski et al., *The Liquid Argon Purity Demonstrator*, 2014 *JINST* **9** P07005 [arXiv:1403.7236].

2026 JINST 21 P11007

[16] R. Andrews et al., *A system to test the effects of materials on the electron drift lifetime in liquid argon and observations on the effect of water*, *Nucl. Instrum. Meth. A* **608** (2009) 251.

[17] I. Badhrees et al., *Argontube: An R&D liquid Argon Time Projection Chamber*, 2012 *JINST* **7** C02011.

[18] A. Ereditato et al., *Design and operation of ARGONTUBE: a 5 m long drift liquid argon TPC*, 2013 *JINST* **8** P07002 [arXiv:1304.6961].

[19] CAPTAIN collaboration, *The Mini-CAPTAIN liquid argon time projection chamber*, *Nucl. Instrum. Meth. A* **1001** (2021) 165131 [arXiv:2008.11422].

[20] DUNE collaboration, *Spatial and temporal evaluations of the liquid argon purity in ProtoDUNE-SP*, 2025 *JINST* **20** P09008 [arXiv:2507.08586].

[21] G. Carugno, B. Dainese, F. Pietropaolo and F. Ptohos, *Electron lifetime detector for liquid argon*, *Nucl. Instrum. Meth. A* **292** (1990) 580.

[22] S.J. Fogarty, *Development of a liquid argon purity monitoring system*, M.Sc. thesis, Colorado State University, Fort Collins, CO, U.S.A. (2023).

[23] D. Nygren and Y. Mei, *Q-Pix: Pixel-scale Signal Capture for Kiloton Liquid Argon TPC Detectors: Time-to-Charge Waveform Capture, Local Clocks, Dynamic Networks*, arXiv:1809.10213.

[24] J. Asaadi, D.A. Dwyer and B. Russell, *Novel Liquid Argon Time-Projection Chamber Readouts*, *Ann. Rev. Nucl. Part. Sci.* **74** (2024) 529.

[25] J. Grigat, D. Masson and M. Schumann, *Doberman: a modular and distributed slow control system for small- to medium-scale experiments*, 2026 *JINST* **21** P07011 [arXiv:2602.04580].

[26] D. Masson and J. Grigat, *Doberview*, https://github.com/AG-Schumann/doberview.

[27] L. Manenti et al., *Performance of different photocathode materials in a liquid argon purity monitor*, 2020 *JINST* **15** P09003 [*Erratum ibid.* **15** (2020) E11001] [arXiv:2005.08187].

[28] Y. Li et al., *Parameterization of electron attachment rate constants for impurities in LArTPC detectors*, 2022 *JINST* **17** T11007 [arXiv:2205.06888].

2026 JINST 21 P11007